Advanced spectroscopic analysis of 0.8—1.0-MA Mo *x* pinches and the influence of plasma electron beams on *L*-shell spectra of Mo ions

A. S. Shlyaptseva, S. B. Hansen, V. L. Kantsyrev, D. A. Fedin, and N. Ouart
Physics Department/220, University of Nevada, Reno, Nevada 89557

K. B. Fournier
Lawrence Livermore National Laboratory, Livermore, California 94550

U. I. Safronova
Department of Physics, University of Notre Dame, Notre Dame, Indiana 46566
(Received 24 August 2002; published 13 February 2003)

This paper presents a detailed investigation of the temporal, spatial, and spectroscopic properties of *L*-shell radiation from 0.8 to 1.0 MA Mo *x* pinches. Time-resolved measurements of x-ray radiation and both time-gated and time-integrated spectra and pinhole images are presented and analyzed. High-current *x* pinches are found to have complex spatial and temporal structures. A collisional-radiative kinetic model has been developed and used to interpret *L*-shell Mo spectra. The model includes the ground state of every ionization stage of Mo and detailed structure for the O-, F-, Ne-, Na-, and Mg-like ionization stages. Hot electron beams generated by current-carrying electrons in the *x* pinch are modeled by a non-Maxwellian electron distribution function and have significant influence on *L*-shell spectra. The results of 20 Mo *x*-pinch shots with wire diameters from 24 to 62 μm have been modeled. Overall, the modeled spectra fit the experimental spectra well and indicate for time-integrated spectra electron densities between 2×10^{21} and 2×10^{22} cm^{-3}, electron temperatures between 700 and 850 eV, and hot electron fractions between 3% and 7%. Time-gated spectra exhibit wide variations in temperature and density of plasma hot spots during the same discharge.

DOI: 10.1103/PhysRevE.67.026409 PACS number(s): 52.58.Lq, 32.30.Rj, 52.70.La

I. INTRODUCTION

An *x*-pinch plasma is formed by touch-crossing two wires between the output electrodes of a high-current pulsed-power generator [1]. The high current quickly vaporizes and strongly ionizes the wire material. The *x* pinch yields short x-ray bursts from a small bright spot or spots at the intersection of the crossed wires. *x* pinches are a good source for developing 1–10 keV x-ray backlighters [2–4], are possible candidates for 50–100 keV x-ray backlighters [5,6], and can be used for testing x-ray spectropolarimetry (a powerful tool for studying the anisotropy of high-temperature plasma) [7] and other applications. In earlier studies, *x* pinches have been made from Al to Pd materials, and in most studies at Cornell University (USA) and Physical Lebedev Institute (Russia), they have been driven by currents of 0.1–0.4 MA with rise times of about 100 ns [1,3,4]. At higher currents around 1 MA, the authors are only aware of three *x*-pinch-related publications: an Al x-pinch driven by 1.0 MA with a rise time of 90 ns [2], Ti and Fe *x* pinches [5,7], and one preliminary report on the results of an x-ray and hard x-ray studies of Ti, Fe, Mo, W, and Pt *x* pinches with currents of 0.9–1.0 MA and a rise time of 100 ns [6]. The Mo *x*-pinch experiments presented here were performed on the pulsed-power machine at the Nevada Terawatt Facility, which operates with a peak current of 0.8–1.0 MA, a rise time of 100 ns, a maximum stored energy of 200 kJ, and a 1.9 Ω pulse-forming line impedance.

This paper presents the time-integrated and time-resolved experimental results of two Mo *x*-pinch shots in detail and summarizes the time-integrated analysis of 20 shots. It should be emphasized that while hot electron effects have been studied for Al and Ar ions [8,9], here we study their effects on higher-*Z* (Mo) ions. In Sec. II, the experimental investigations of the spatial, temporal, and spectral structures of Mo *x* pinches are presented. Section III presents the details of the atomic kinetic model used to diagnose the electron temperature, density, and electron beam characteristics of the *x*-pinch plasmas by the comparison of modeled spectra to experimental spectra. The dDiscussion and the summary are given in Secs. IV and V, respectively.

II. EXPERIMENTAL RESULTS

A. Temporal structure of x-ray bursts

In the experiments described here, the temporal behavior of x-ray bursts was studied with a side-on filtered absolutely calibrated photoconducting diode (PCD), a vacuum x-ray diode with a Ni mesh and a C cathode (XRD) (both provided by Sandia National Laboratories), and a Tektronix TDS 640 2 gigasample (GS)/s digital oscilloscope with 0.5 ns time resolution. Different filter combinations were applied to measure power and energy estimates with different photon energies. For example, for the 50 μm Mo *x*-pinch shot with 0.95 MA peak current, the PCD filtered with 25 μm kapton (which has a low-energy cutoff determined by a 10% transmission level of $\lambda_{1/10}<7.9$ Å) recorded several 1.1 ns pulses with estimated energies of 20–30 J and powers up to 3×10^{10} W. For the same shot, the XRD filtered with 8-mm Be ($\lambda_{1/10}<17$ Å) recorded 1.2 ns pulses with estimated energies of 250–350 J and powers up to $(2-3)\times10^{11}$ W. An

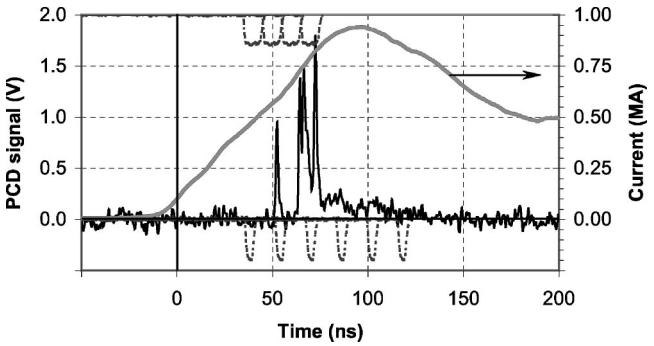

FIG. 1. Load current, soft x-ray PCD signal, and MCP frames for the time-resolved spectrometer 1DXIS (top) and time-resolved pinhole camera (bottom) for a planar loop 62 μm Mo *x* pinch (shot 84).

unfiltered, absolutely calibrated Ni bolometer was used to estimate the total yield of x ray and extreme ultraviolet radiation up to 10 kJ [5,6].

Load currents, soft x-ray PCD signals, and microchannel plate (MCP) frames for the time-resolved spectrometer 1DXIS and pinhole camera are shown for 62 μm (Fig. 1) and 50 μm (Fig. 2) Mo *x* pinches. Three major x-ray bursts were observed for the 62 μm *x* pinch. In contrast, for the 50 μm *x* pinch, only one major burst appears along with a few minor bursts.

B. Spatial structure of *x*-pinch plasma

For x-ray imaging of *x*-pinch plasmas, three different imaging systems were used. Specifically, a side-on time-integrated survey low-resolution pinhole camera generated three plasma images behind three different filters ($\lambda_{1/10}<2.6$ Å, $\lambda_{1/10}<7.9$ Å, and $\lambda_{1/10}<5$ Å). The diameter of pinholes in the gold membrane was 100 μm, the spatial resolution was 580 μm, and the magnification was 0.5. The images were registered on Kodak DEF-5 (direct exposure film) x-ray film. The second imaging system was a side-on time-integrated high-resolution pinhole camera, which generated two plasma images behind two different filters ($\lambda_{1/10}<3.5$ Å and $\lambda_{1/10}<10$ Å). The spatial resolution of this device was 72 μm and the magnification was about 0.71. These images were also registered on Kodak DEF-5 x-ray

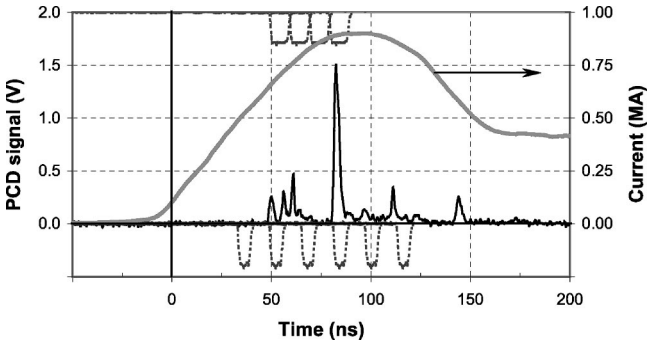

FIG. 2. Load current, soft x-ray PCD signal, and MCP frames for the time-resolved spectrometer 1DXIS (top) and time-resolved pinhole camera (bottom) for a planar loop 50 μm Mo *x* pinch (shot 92).

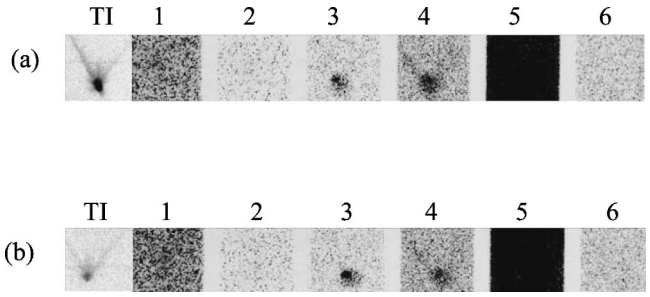

FIG. 3. X-ray images from a 62 μm Mo *x* pinch (shot 84). Time-integrated (TI) and time-gated pinhole images (1-6) at $\lambda_{1/10}<3.5$ Å (a) and $\lambda_{1/10}<10.5$ Å (b). For time-gated pinhole images, the duration of the frame was 4 ns, the interval between the beginning of frames was 17 ns, and the spatial resolution was 230 μm.

film. Finally, a side-on multichannel time-gated pinhole camera has been used. This camera had six time frames with adjustable discrete intervals from 1 to 8 ns with an increment of 1 ns; the interval between the beginning of frames could be adjusted from 1 to 20 ns. The magnification was 0.5 and the distance from the plasma to the filtered pinholes was 70 cm. One 25 μm or 50 μm Be filter protected membranes from plasma debries damage. The diameter of holes in the two identical parallel rows of Pt/Ir membranes was 30 or 70 μm and there were six membranes in each row. The spatial resolution of the pinhole-MCP system was 130 or 250 μm, respectively. Two rows of images were formed on MCP frames by placing two different combinations of Cr or Mylar filters in front of the pinholes. One row had 3 μm Mylar and 0.2 μm Al filters to record images for $\lambda_{1/10}<10$ Å, and the other had 2 μm Cr and 170 μm Mylar filters to record images for $\lambda_{1/10}<3.5$ Å. Diffraction limits spatial resolution for side-on diagnostics to 20–25 μm at $\lambda=10$ Å and 5–10 μm at $\lambda=1$ Å due to the large distance from plasma to detectors (>30–60 cm).

The spatial structure of *x* pinches driven by high current is more complicated than that of low-current *x* pinches [3,4]. Figures 3 and 4 show time-gated pinhole images for 62 and 50 μm Mo wire loads, respectively, which correspond to the MCP pinhole frames indicated in Figs. 1 and 2. For the 62 μm load (Fig. 3), the structure of the central spot at the

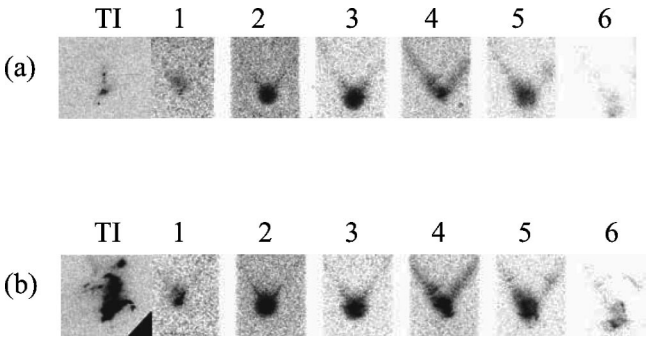

FIG. 4. X-ray images from a 50 μm Mo *x* pinch (shot 92). Time-integrated (TI) and time-gated pinhole images (1–6) at $\lambda_{1/10}<3.5$ Å (a) and $\lambda_{1/10}<10.5$ Å (b). For time-gated pinhole images, the duration of the frame was 4 ns, the interval between the beginning of frames was 17 ns, and the spatial resolution was 230 μm.

crossing point of the wires is more uniform than that of the 50 μm load (Fig. 4). In Fig. 3, frames 1 and 5 are saturated. This indicates strong hard x-ray emission which may be due to strong electron beams. In Fig. 4, plasma jets are evident in frames 3 through 5, which also indicates strong electron beams. Note that in Fig. 4, the plasma jets are directed not only along the discharge axis but also perpendicular to the initial position of the wires [5]. In the time-integrated pinhole image of the 50 μm *x* pinch (Fig. 4), five separate hot spots are resolved. In contrast, only one hot spot is resolved in the time-integrated pinhole image of the 62 μm pinch (Fig. 3).

C. Spectroscopy of *x* pinches

Mo *L*-shell spectra were recorded using two different devices. A wide spectral region with spatial resolution was registered with a side-on one-dimensional x-ray time-integrated convex-crystal spectrometer. The crystals in this spectrometer were convex potassium hydrogen phthalate (KAP) ($2d = 26.62$ Å and radius of curvature$= 25.4$ mm) or α quartz ($2d = 6.687$ Å and radius of curvature$= 102$ mm). The plane of dispersion of the spectrometer was perpendicular to the axis of the *z*-pinch discharge. Due to the low luminosity of convex spectrometers, a spatial resolution of only 7 mm has been achieved by placing a 1 mm Pb slit protected from the plasma by a 15 μm Be filter with a 3 μm Mylar back coating. Such a resolution is sufficient to show differences between spectra near the anode, in the central region of *x* pinch, and near the cathode. These regions are of most interest because the x-ray plasma images indicate a point-type source of the pinch in the central region. Spectra were registered on Kodak DEF-5 x-ray film with a double 3 μm Mylar filter with 0.2 μm Al coating. The operating wavelength range for the spectrometer was $\lambda < 15$ Å and the resolution $\lambda/\Delta\lambda$ was 700–800.

Time-resolved spectra were obtained in a narrow spectral region with a side-on time-gated flat crystal spectrometer [5] with a multistrip Galileo MCP imager. For the Mo experiments, an α-quartz crystal with $2d = 6.687$ Å was used. The distance between the plasma and crystal was 100 cm. For the α-quartz crystal, the observation range in one shot was ± 0.25 Å near the central wavelength 4.55 Å with resolution $\lambda/\Delta\lambda = 800$–$1000$. The crystal was protected from the plasma by a 50 μm Be filter with a 5 μm Mylar back coating. The x-ray spectra were registered on a six-strip MCP x-ray imager with a 40 mm diameter. The MCP was protected by a double 3 mm Mylar filter with a 0.2 mm Al coating. Due to geometrical limitations, only four of the six strips were used. The temporal resolution (duration of frames) and the interval between the beginning of frames can be adjusted from 1 to 9 ns and from 3 to 20 ns, respectively. The optical image of x-ray spectra output from the MCP was registered on Kodak Pan film 2484.

Time-gated MCP spectra of the 62 and 50 μm wire loads are shown in Figs. 5(a) and 5(b), respectively. The MCP frames for these shots are indicated at the top of Figs. 1 and 2. For the 62 μm load, the MCP frames 2,3, and 4 capture and resolve the first three x-ray bursts. For the 50 μm load, two MCP frames 2 and 4 capture emission from separate x-ray bursts while frame 4 records the major burst. There is a significant variation in the MCP spectra from the different bursts. Experimental spectra were calibrated using theoretical wavelengths and experimental intensities were found in photons/cm^2. The spectra are analyzed and discussed in Sec. III below.

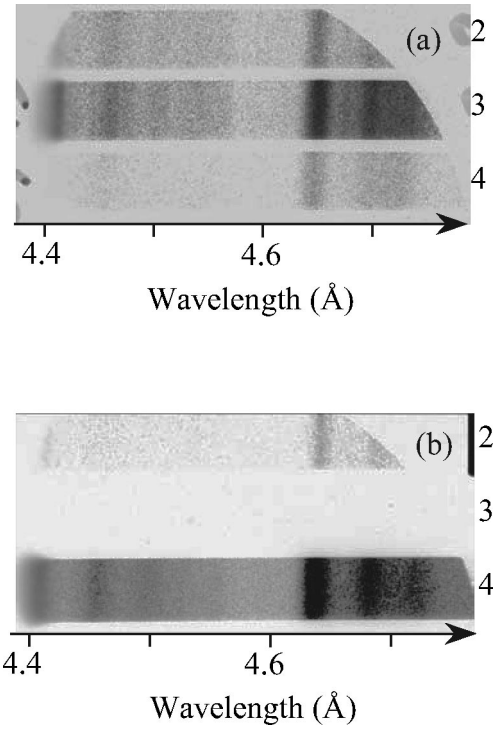

FIG. 5. Time-gated x-ray spectra from two Mo *x*-pinch shots with a different wire diameter: (a) 62 μm (shot 84) and (b) 50 μm (shot 92). The duration of frames was 8 ns and the interval between the beginning of frames was 9 ns.

III. MODELING AND DIAGNOSTICS

A. Kinetic model

A collisional-radiative kinetic model was developed to diagnose the Nevada Terawatt Facility (NTF) experimental Mo *L*-shell spectra. In this section, the model structure, data sources, rate calculations, and the selection of spectral features used for diagnostics are discussed. The kinetics model produces synthetic spectra that are dependent on plasma conditions represented by three parameters: electron temperature (T_e), electron density (n_e), and the fraction of hot electrons (f). By comparison with experimental spectra, the conditions of the x-ray source can be inferred.

The kinetic model includes the ground state of all ions from neutral to bare Mo, for which ionization potentials were taken from published tables [10,11]. A detailed structure for O-like to Mg-like Mo ions includes singly excited states up to $n = 7$ for O- through Ne-like ions and both singly and doubly excited states up to $n = 4$ for Na- and Mg-like ions. Energy level structures and complete radiative and collisional coupling data were calculated by the HULLAC suite of atomic structure codes [12,13]. Selected energy levels and radiative decay rates in the Ne-like ion were calculated to

high accuracy with many-body perturbation theory [14]. Supplemental modified Lotz collisional ionization strengths [15] and Kramers radiative recombination are used where the HULLAC data is not avaliable. To increase the speed of calculation, levels with $n>3$ in the Mg-, Na-, F-, and O-like ions have been configuration averaged [16]. We have found that such averaging gives level populations that are in a good agreement with the nonaveraged model.

All collisional rates are calculated by integrating collision cross sections over an electron distribution function. It is composed of both Maxwellian and non-Maxwellian portions: $F(\varepsilon)=(1-f)F_m(\varepsilon)+fF_{nm}(\varepsilon)$. Here, ε is the electron energy, f is the fraction of non-Maxwellian hot electrons, F_m is a Maxwellian distribution at the bulk plasma electron temperature T_e, and F_{nm} is a non-Maxwellian distribution [17]. The fraction f of non-Maxwellian electrons represents hot electrons in the current-carrying beam of the *x* pinch. Measurements of hard x rays [6,18] indicate that the main portion of hot electrons in Mo *x* pinches are spread over a wide range of energies and persist up to energies of 40–50 keV. To account for this observation, the hot electrons are modeled by a distribution function given by $F_{nm}=C\varepsilon^{-3}$ for electrons with energy ε greater than the cutoff energy $\varepsilon_0=10$ keV (C is a normalization coefficient).

The spontaneous and collisional rates between all modeled levels form a set of coupled rate equations. Solving the coupled rate equations with standard matrix methods determines steady-state level populations. The intensity of a spectral line is given by product of the population of the upper level and the radiative decay rate of the transition. The synthetic spectrum is the sum of Voigt profiles whose widths are informed by the ion temperature ($T_i=T_e$) and the sum of spontaneous rates from the upper and lower levels of each transition along with two variable broadening factors. The broadening factors are the same for all spectral lines in a given spectrum and are determined independently for each experimental spectrum by the best fit to the well-resolved Ne-like $3G$ line.

B. Effects of parameters on modeled spectra

Figure 6 shows the *L*-shell spectral region of interest decomposed into contributions from ionization stages O- through Mg-like Mo. The Ne-like lines, labeled with their traditional names, are single transitions, while features from the surrounding ionization stages are composed of many lines. The Ne-like $3A$ and $3B$ lines are transitions from $2s2p^6 3p$ states to the Ne-like $2s^2 2p^6$ ground state, the $3C$ and $3D$ lines are transitions from $2s^2 2p^5 3d$ to the ground state, and the $3F$ and $3G$ lines are transitions from the low-lying $2s^2 2p^5 3s$ states to the ground state. The experimental spectra are diagnosed using a subset of the labeled features and lines: the F-like feature at 4.5 Å (F1), the Ne-like $3A$, $3B$, $3F$, and $3G$ lines, the Na-like satellite feature at 4.844 Å (Na1), and the Mg-like satellite feature at 4.88 Å (Mg1). This selection notably excludes prominent spectral lines and features such as the Ne-like $3D$ and $3C$ lines and the combined Na-like (Na2) and F-like (F2) features at 4.644 Å. However, the limited selection has several advantages. The selected features are relatively isolated from emission from other ionization stages, so their parameter dependence can be well characterized. Determining three plasma parameters with only three line ratios prevents overdetermination of the system and the fit of spectral features that are not explicitly optimized act as checks of the fit quality. We note that the diagnostic ratios presented below are either ratios of lines to lines or features to features. Thus, they are much less sensitive to variations in linewidths than ratios that include a mix of single lines and composite features. Figure 7 shows the ionization balance of the Mo plasma as a function of T_e at $n_e=10^{22}$ cm^{-3}. The relative intensity of spectral features from different ionization stages in the modeled spectra reflect the dependence of the ionization balance on T_e. The ionization balance is also sensitive to the fraction of hot electrons f, as shown in Fig. 7(b), which gives the ionization balance as a function of T_e with $n_e=10^{22}$ cm^{-3} and $f=5\%$. Hot electrons decrease the bulk temperature needed to reach high charge states and can populate a wider range of ionization stages than is possible by variation in T_e alone.

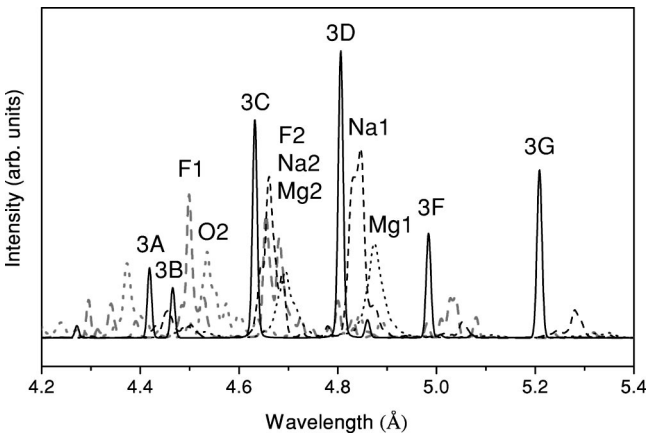

FIG. 6. Contributions of O-like (dotted gray line), F-like (dashed gray line), Ne-like (solid black line), Na-like (dashed black line), and Mg-like (dotted black line) Mo ions to the *L*-shell synthetic spectrum.

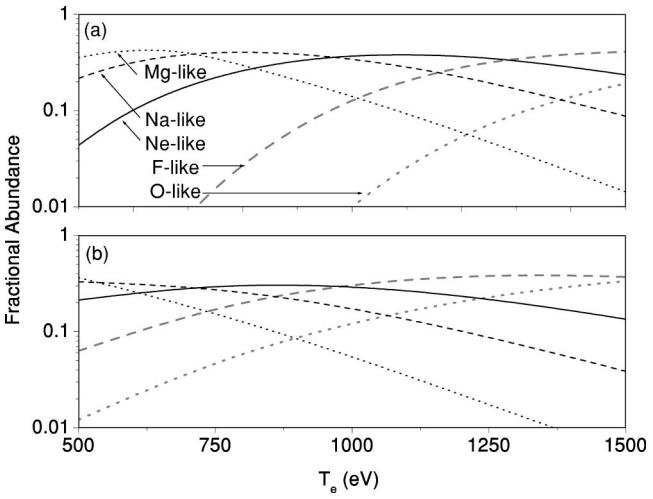

FIG. 7. Ionization balance curves for $n_e=10^{22}$ cm^{-3} as a function of T_e with no hot electrons (a) and with 5% hot electrons (b).

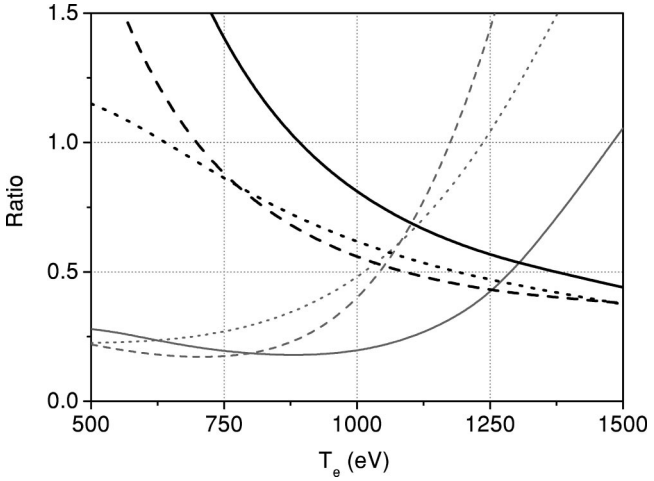

FIG. 8. Ratios of Mg1/Na1 (black lines) and F1/Na1 (gray lines) features as a function of T_e for $n_e=10^{22}$ cm^{-3}. Solid lines have $n_e=10^{21}$ cm^{-3} and no hot electrons, dashed lines have $n_e=10^{22}$ cm^{-3} and no hot electrons, and dotted lines have $n_e=10^{21}$ cm^{-3} and 5% hot electrons.

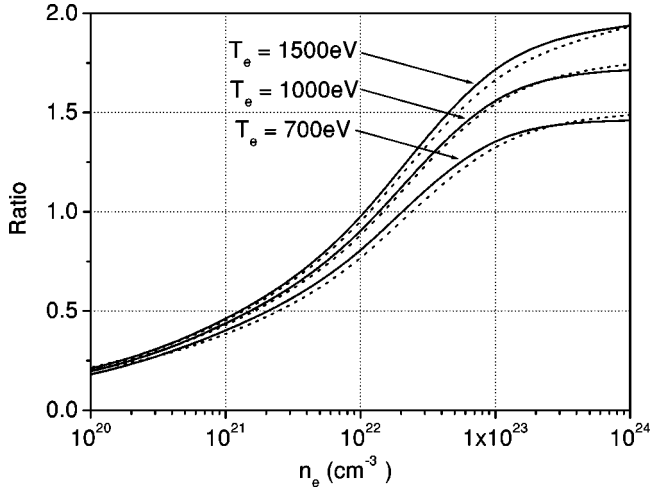

FIG. 9. Ratios of the Ne-like lines $(3A+3B)/(3F+3G)$ as a function of n_e for $T_e=700$, 1000, and 1500 eV. Solid lines have no hot electrons, dotted lines have 5% hot electrons. Local thermodynamic equilibrium ratios for $T_e=700$, 1000, and 1500 eV are 1.5, 1.76, and 2.0, respectively.

Hot electrons affect not only the ionization balance and thus the relative emission between ionization stages, they also affect the relative intensities of lines within single ionization stages. In particular, hot electrons tend to increase the intensities of high-energy satellites in the Na- and Mg- like emission features and to decrease the intensities of $3D$ and $3C$ relative to the other Ne-like lines. It should be noted that the latter effect is not seen with models that include only $n=3$ states in the Ne-like ion [19]. The Mg- and Na-like satellite features are not sufficiently resolved in most of the spectra presented here for their dependence on hot electrons to be diagnostically useful. The ratios of the features Mg/Na and F/Na are given in Fig. 8 as a function of T_e for three cases: $n_e=10^{21}$ and 10^{22} cm^{-3} with no hot electrons and $n_e=10^{21}$ cm^{-3} with 5% hot electrons. Figure 8 shows that a few percent of hot electrons have effects similar to increasing n_e by an order of magnitude or T_e by several hundred eV. Also, larger Mg1/Na1 and F1/Na1 ratios can be reached simultaneously with hot electrons than with variation of T_e and n_e alone.

Figure 8 illustrates that increasing electron density increases the ionization balance of the plasma. More importantly for diagnostic purposes, the electron density also affects the relative intensity of lines within single ionization stages. The effect of the electron density on the Ne-like lines is especially pronounced. The strong Ne-like $3s$-$2p$ ($3F$ and $3G$) and $3p$-$2s$ ($3A$ and $3B$) transitions have been used previously as density diagnostics [20,21]. The intensities of the low-lying $3G$ and $3F$ lines depend on radiative cascades from highly excited states in the Ne-like ion. As the electron density increases, these radiative cascades are disrupted by collisional processes and the relative intensities of the $3G$ and $3F$ lines decrease. In contrast, the intensities of the $3A$ and $3B$ lines depend more directly on collisional excitation and increase with increasing n_e. Thus, the ratio $(3A+3B)/(3G+3F)$ increases monotonically with n_e, as shown in Fig. 9. This line ratio is independent of the ionization balance and fairly insensitive to f (as shown by the dotted lines in Fig. 9 which have $f=5\%$) and is thus an excellent density diagnostic.

C. Diagnostics of time-integrated spectra

Without hot electrons, the two parameters T_e and n_e can be simultaneously determined by two ratios: the $(3A+3B)/(3F+3G)$ ratio of Ne-like lines and either the Mg1/Na1 or the F1/Mg1 ratio. For either of these ratios, the precision of the predicted temperatures and densities are about 5% and 30%, respectively. However, the predicted temperatures given by these two ratios do not agree for the Mo x-pinch spectra. The T_e predicted by the F1/Na1 ratio is in general 200–300 eV greater than the T_e predicted by the Mg1/Na1 ratio. Thus, the two parameters T_e and n_e are generally not sufficient to fit the Mo x-pinch experimental spectra. The deficiency of the two-parameter model is illustrated in Fig. 10(a), which shows the best two-parameter fit to an x-pinch spectrum. The Mg-, Na-, and Ne-like features fit the experiment well, but the modeled F-like feature does not have sufficient intensity. If the temperature is increased to bring the F1 feature into a better agreement with the experiment, the fit of the Mg1 features will suffer. The improvement in the fit when hot electrons are included is illustrated in Fig. 10(b), in which a rather large fraction of hot electrons, along with a lower bulk temperature and larger electron density, gives a modeled spectrum that fits the experiment well. The addition of hot electrons to the model decreases the precision of the diagnosed parameters; n_e can still be determined to within 30% and T_e and f can be determined to within only about 20%.

Fits of three Mo x-pinch spectra with wire diameters from 62, 50, and 24 μm are given in Fig. 11. The fit of the model to the experiments is generally good. The two shots shown here for the 50 and 62 μm wire are the same shots discussed in Sec. II, whose time-gated spectra will be analyzed

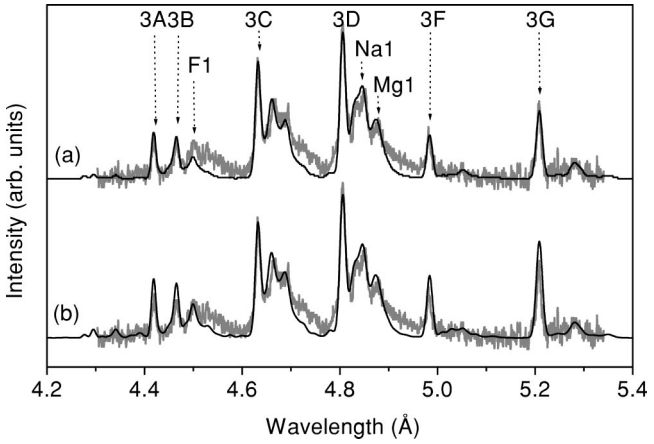

FIG. 10. Experimental time-integrated spectrum (gray lines) from 35.3 μm Mo *x*-pinch fit with modeled spectra (black lines). The modeled spectra have (a) $T_e=1025$ eV and $n_e=4\times10^{21}$ cm^{-3}, and no hot electrons; and (b) 5.5% hot electrons, $T_e=750$ eV, and $n_e=5\times10^{21}$ cm^{-3}.

below. The most obvious difference between the spectra shown in Fig. 11 is the relative intensities of the Ne-like $3F$ and $3G$ lines, which decrease with the wire diameter. As explained in Sec. III B, decreasing intensities of $3F$ and $3G$ indicate increasing electron densities. The smallest wire diameter (24 μm) has a diagnosed electron density a full factor of 10 larger than that diagnosed for the largest wire diameter (62 μm). This is representative of a general trend in the data of decreasing density with increasing wire diameter.

The predicted T_e, n_e, and f values for a large set of experimental data are given in Table I, along with the wire diameter, the total current, and the total bolometer and PCD

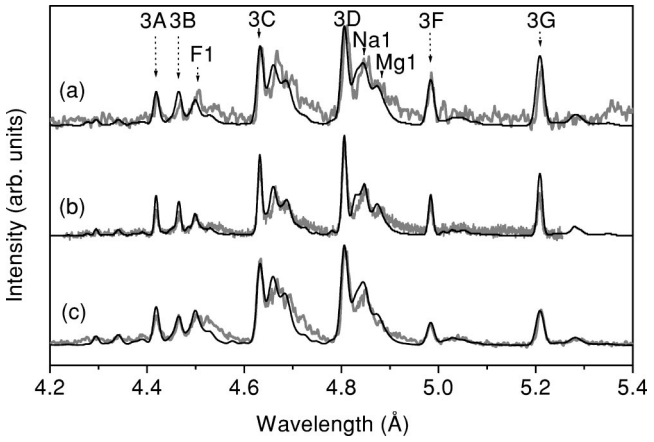

FIG. 11. Experimental time-integrated spectra (gray lines) from Mo *x* pinches of various wire diameters fit with modeled spectra (black lines). In (a) the experimental spectrum is from a 62 μm wire pinch (shot 84) and the modeled spectrum has 7% hot electrons, $T_e=850$ eV, and $n_e=2\times10^{21}$ cm^{-3}. In (b) the experimental spectrum is from a 50 μm wire pinch (shot 92) and the modeled spectrum has 4.5% hot electrons, $T_e=850$ eV, and $n_e=5\times10^{21}$ cm^{-3}. In (c) the experimental spectrum is from a 24 μm wire pinch (shot 60) and the modeled spectrum has 3% hot electrons, $T_e=825$ eV, and $n_e=2\times10^{22}$ cm^{-3}.

energies (where available). Data for three shots with wire diameters of 62 μm and for 15 shots with wire diameters of 50 μm are included, but the two smaller wire diameters (35 and 24 μm) are represented with only one shot each. The large 50 μm dataset shows that the shots are moderately reproducible, with diagnosed temperatures ranging from 700 to 850 eV, diagnosed densities ranging from 2×10^{21} and 9×10^{21} cm^{-3}, and hot electron fractions from 4% and 7% that tend to increase with the measured current. The three 62 μm shots are also fairly reproducible, with temperatures from 800 to 850 eV, densities from 2×10^{21} to 2.5×10^{21} cm^{-3}, and hot electron fractions from 5.5% to 7%. A clear trend of decreasing density with increasing wire diameter can be seen between the well-represented 50 and 62 μm shots, and the higher diagnosed densities of the two smaller diameter wires follow this trend.

D. Diagnostics of time-gated spectra

For a few Mo shots, time-gated spectra were collected along with time-integrated spectra (see Sec. II C). The time-gated spectral images are limited to the region from 4.4 Å to 4.7 Å, which includes the Ne-like $3B$ and $3C$ lines, part of the Ne-like $3A$ line, the F1 structure at 4.5 Å, and the F2/Na2 structure at 4.664 Å. This spectral region contains less information than the full spectral region covered by the time-integrated data and makes precise diagnosis of three parameters difficult. It will be shown that at least one of the time-gated spectra from each shot can be well described by the parameters used to model the time-integrated spectrum from that shot. For the other time-gated spectra only T_e, n_e, and limiting values for f that give agreement with experiment in the available spectral range can be determined.

Figure 12 shows the best fit of modeled spectra to time-gated images from the 62 μm pinch described in Sec. II. For this shot, the MCP picked up emission from all of the well-resolved initial x-ray bursts. The first two frames [Figs. 12(a) and 12(b)] recorded spectra that resemble the time-integrated spectrum. The first spectrum [Fig. 12(a)] is fairly well-described by a modeled spectrum with parameters identical to those found for the time-integrated spectrum. The second spectrum [Fig. 12(b)] has a density similar to the first and a larger temperature (there is insufficient information in this spectral range for a precise determination of f). The last spectrum [Fig. 12(c)] shows only the Ne-like $3D$ line and some Na- and Mg-like features. The absence of the F-like features and the small intensities of the $3A$ and $3B$ lines indicate n_e below 3×10^{19} cm^{-3} and f below 1%. This n_e is notably smaller than that diagnosed for the time-integrated spectrum.

Figure 13 shows the best fit of modeled spectra to time-gated images from the 50 μm pinch (also described in Sec. II). For this shot, only two MCP frames recorded significant spectral emission. The second frame [Fig. 13(a)] recorded a spectrum similar to that of the last frame of the 62 μm pinch with much less line broadening. The narrow lines may indicate that the ions had not yet thermalized. The low-intensity $3A$ and $3B$ lines and the absence of F-like emission again indicate a relatively low density. The satellite lines are suffi-

TABLE I. Experimental data and diagnosed plasma parameters of Mo *x* pinches from time-integrated spectra.

Shot	ψ (μm)	I (MA)	Bolometer energy (J)	PCD energy (J)	n_e 10^{21} (cm^{-3})	T_e (eV)	f (%)
62	24.13	0.73		18.7	20	825	3.0
60	35.3	0.92		34.0	5.0	750	5.5
57	50.0	0.86		6.5	7.0	700	5.0
59	50.0	0.94		45.5	5.0	700	6.5
65	50.0	0.9	8130	14.5	3.0	750	5.5
67	50.0	0.93	6000		4.0	750	6.0
69	50.0	1.0	5610	24.4	5.0	700	7.0
70	50.0	0.93		16.7	3.0	800	6.0
71	50.0	0.93	7400	33.1	9.0	800	4.0
81	50.0	0.88	7400	17.8	5.0	800	4.5
83	50.0	0.83	8780	28.2	2.0	750	6.5
86	50.0	0.94	7640	37.9	2.5	700	7.0
88	50.0	0.95	7160	33.8	3.0	700	6.0
89	50.0	0.98	9550	19.2	4.0	700	5.0
90	50.0	0.9	7680	26.4	5.0	800	6.0
92	50.0	0.89	8640	31.5	5.0	850	4.5
93	50.0	0.93	9760	41.1	3.0	750	6.5
52	61.98	0.9	11200	14.8	2.0	800	5.5
54	61.98	0.9		14.7	2.5	800	5.0
84	61.98	0.96	7920	10.8	2.0	850	7.0

ciently resolved in this spectrum to be useful as hot electron diagnostics: the dominance of lower-energy satellites indicates that the hot electron fraction f is below 0.5%. The fourth frame of the 50 μm pinch [Fig. 13(b)] recorded the main x-ray peak. The recorded spectrum has broader lines and can be fit with the same parameters used to fit the time-integrated spectrum for the same pinch.

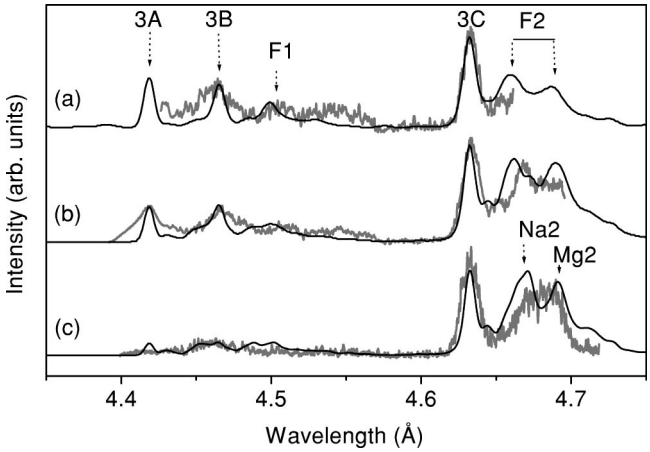

FIG. 12. Time-gated experimental spectra (gray lines) from a 62 μm wire pinch (shot 84) fit with modeled spectra (black lines). Experimental spectra recorded by the frames 2, 3, and 4, respectively, are fit with modeled spectra with (a) 7% hot electrons, $T_e = 850$ eV, and $n_e = 2\times10^{21}$ cm^{-3}; (b) no hot electrons, $T_e = 900$ eV, and $n_e = 10^{21} cm^{-3}$; and (c) no hot electrons, $T_e = 950$ eV, and $n_e = 10^{19}$ cm^{-3}.

The time-dependent PCD measurements (Figs. 1 and 2) illustrate that these high-current *x*-pinch implosions are not smooth and predictable, but are rather characterized by a succession of x-ray bursts. The analysis of time-gated spectra indicate that these x-ray bursts themselves are not uniform, and probably arise from different hot spots formed near the crossing of the *x*-pinch wires. The time-gated spectra fall into two broad categories: those characterized by large tempera-

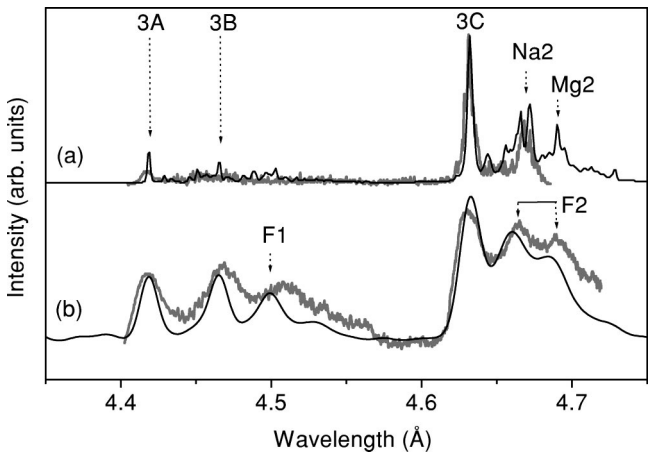

FIG. 13. Time-gated experimental spectra (gray lines) from a 50 μm wire pinch (shot 92) fit with modeled spectra (black lines). Experimental spectra recorded by the frames 2 and 4, respectively, are fit with modeled spectra with (a) no hot electrons, $T_e = 1100$ eV, and $n_e = 10^{19}$ cm^{-3} and (b) with 4.5% hot electrons, $T_e = 850$ eV, and $n_e = 5\times10^{21}$ cm^{-3}.

tures, densities, and significant fractions of hot electrons; and those with much lower densities and negligible fractions of hot electrons.

IV. DISCUSSION

Analysis of the largest sample of shots of 50 μm wire loads indicates that the diagnosed fraction of hot electrons tends to increase with the current, which supports their modeled role as current-carrying beams. Larger fractions of hot electrons also correlate with lower electron densities and lower bulk temperatures, which suggests a competition between the energy carried by the hot electrons and the energy deposited in the hot spots.

Analysis of the two time-gated spectra shows much wider variation in plasma parameters than indicated by the time-integrated spectra. The correlation of time-gated spectra with the x-ray bursts of these two *x* pinches provides insight into their temporal structure and can help to refine the interpretation of time-integrated spectra. Time-integrated spectra are usually taken to be representative of the most emissive part of the pinch. This interpretation is adequate for the 50 μm *x* pinch (shot 92), where the most intense x-ray burst accounts for around 25% of the total PCD energy and has a spectrum that is very similar to the time-integrated spectrum. In contrast, the most intense x-ray burst of the 62 μm *x* pinch (shot 84) accounts for only 10% of the total PCD energy and has a spectrum with a very different character from that of the time-integrated spectrum. The time-integrated spectrum is instead similar to spectra from the x-ray bursts preceding the main burst. Unfortunately, no information is available on the character of *L*-shell emission from the long string of weak bursts that follow the main burst. A comprehensive analysis of time-gated spectra is planned to investigate these issues further.

The spectroscopic analysis presented here can also be used to infer the characteristic size of hot spots in *x* pinches, a matter of recent interest to the pulsed-power community. While the pinhole imaging systems in considered experimental geometry cannot resolve anything below 70 μm, the spectroscopic diagnostics indicate a hot spot size on the order of 10 μm. Two independent estimates of the hot spot size have been made using results of the spectroscopic analysis. First, the densities are so high that the spectra from any hot spot larger than 10–50 μm will be affected by line absorption. The first manifestation of opacity effects would be a reduction in intensity of the strong $3D$ and $3C$ Ne-like lines relative to other spectral lines and features. Since the modeled optically thin spectra fit these experimental Ne-like lines well, even without being optimized to fit them, it is probable that the hot spots are smaller than about 50 μm. A second estimate of the hot spot size can be made by comparing the measured *L*-shell emission of a single x-ray burst with the modeled *L*-shell emission integrated over 1–2 ns. The latter quantity is dependent on the emitting plasma volume. This estimate predicts a hot spot size of 10–30 μm. Both estimates are consistent with the estimated sizes of hot spots in Mo line emission spectral region in Refs. [3,4].

V. SUMMARY

The temporal, spatial, and spectral structures of a number of Mo *x*-pinch shots have been investigated with advanced x-ray diagnostics and a detailed atomic kinetic model.

Plasma parameters for 20 Mo *x*-pinch shots with wire diameters from 24 to 62 μm have been diagnosed from time-integrated spectra. The spectroscopic kinetics model incorporates a non-Maxwellian electron distribution to represent current-carrying electrons, which are evidenced by pinhole images, holes in the anode, and hard x-ray measurements. Hot electrons are shown to have significant effects on modeled spectra and tend to correlate well with measured load currents. For time-integrated spectra, diagnosed fractions of hot electrons range from 3% to 7% and bulk electron temperatures range from 700 to 850 eV. Diagnosed electron densities range from 2×10^{21} to 2×10^{22} cm^{-3}, with smaller wire diameters having larger diagnosed electron densities.

Time-resolved records of plasma x-ray emission from two shots with diameters of 62 and 50 μm show several x-ray bursts during the pinch evolution. These x-ray bursts are thought to arise from separate hot spots in the *x*-pinch plasmas. Spectroscopic analysis of time-gated spectra shows that the different x-ray bursts may arise from plasma regions with widely different conditions. For the time-gated spectra, diagnosed electron densities range between 10^{19} and 2×10^{21} cm^{-3}, bulk electron temperatures range from 850 to 1100 eV, and hot electron fractions reach 7%. Two independent estimates indicate that the hot spots have sizes on the order of 10 μm.

ACKNOWLEDGMENTS

The authors acknowledge in particular, K. Struve, C. Deeney, T. Nash, and J. McGurn from Sandia National Laboratories, whose work and help is excerpted in this paper. We acknowledge the program support by B. Bauer, measurements of load and stack currents by R. Presura, and experimental help from S. Batie, H. Faretto, S. Fuelling, B. LeGalloudec, A. Oxner, and S. Rogowski. This work was supported by DOE-NNSA/NV cooperative agreement DE-FC08-01NV14050, SNL, and UNR. The work of K.B.F. was performed under the auspices of U.S. Department of Energy by University of California Lawrence Livermore National Laboratory under Contract No. W-7405-Eng-48. U.I.S. acknowledges partial support by Grant No. B156156 from Lawrence Livermore National Laboratory.

[1] S. Zakharov, G.V. Ivanenkov, A.A. Kolomenskii, S.A. Pikuz, and A.I. Samokhin, J. Plasma Phys. **13**, 115 (1987).
[2] D.H. Kalantar, D.A. Hammer, and K.C. Mittal, J. Appl. Phys. **73**, 8134 (1993).
[3] T.A. Shelkovenko, D.B. Sinars, S.A. Pikuz, and D.A. Hammer, Phys. Plasmas **8**, 1305 (2001).
[4] D.B. Sinars, S.A. Pikuz, T.A. Shelkovenko, K.M. Chandler, and D.A. Hammer, Rev. Sci. Instrum. **72**, 2948 (2001).
[5] V. Kantsyrev*et al.*, Rev. Sci. Instrum. **72**, 663 (2001).
[6] V.L. Kantsyrev*et al.*, Proc. SPIE **4502**, 62 (2001).
[7] A.S. Shlyaptseva, S.B. Hansen, V.L. Kantsyrev, B.S. Bauer, D.A. Fedin, N. Ouart, S.A. Kazantsev, A.G. Petrashen, and U.I. Safronova, Rev. Sci. Instrum. **72**, 1241 (2001).
[8] J. Abdallah, A.Y. Faenov, D. Hammer, S. Pikuz, G. Csanak, and R.E.H. Clark, Phys. Scr. **53**, 705 (1996).
[9] J. Abdallah, R.E.H. Clark, A.Y. Faenov, L. Karpinski, S.A. Pikuz, V.M. Romanova, M. Sadowski, M. Sholz, and A. Szydlowski, J. Quant. Spectrosc. Radiat. Transf. **62**, 85 (1999).
[10] E. Biemont, Y. Fremat, and P. Quinet, At. Data Nucl. Data Tables **71**, 117 (1999).
[11] T.A. Carlson, J.C. Nestor, N. Wasserman, and J.D. McDowell, Oak Ridge National Laboratory Report No. 4562, 1970 (unpublished).
[12] M. Klapish, J.L. Shwob, B.S. Fraenkel, and J. Oreg, J. Opt. Soc. Am. **67**, 148 (1977).
[13] A. Bar-Shalom, M. Klapisch, and J. Oreg, Phys. Rev. A **38**, 1773 (1988).
[14] U.I. Safronova, C. Namba, I. Murakami, W.R. Johnson, and M.S. Safronova, Phys. Rev. A **64**, 012507 (2001).
[15] V.A. Bernshtam, Y.V. Ralchenko, and Y. Maron, J. Phys. B **33**, 5025 (2000).
[16] O. Peyrusse, J. Phys. B **32**, 683 (1999).
[17] R. Epstein, S. Skupsky, and J. Delettrez, J. Quant. Spectrosc. Radiat. Transf. **35**, 131 (1986).
[18] V.L. Kantsyrev *et al.*, in *Proceedings of the IEEE Conference on Pulsed Power Plasma, Las Vegas, Nevada*, edited by R. Reinovsky and M. Newton (IEEE, New York, 2001), Vol. 1, p. 346.
[19] A.S. Shlyaptseva, S.B. Hansen, V.L. Kantsyrev, B.S. Bauer, D.A. Fedin, N. Ouart, S. Keely, H. LeBeau, and U.I. Safronova, in *Proceedings of the IEEE Conference on Pulsed Power Plasma* (Ref. [18]), p. 753.
[20] U. Feldman, J.F. Seeley, and A.K. Bhatia, J. Appl. Phys. **58**, 3954 (1985).
[21] A. Dasgupta, K.G. Whitney, H.L. Zhang, and D.H. Sampson, Phys. Rev. E **55**, 3460 (1997).